Modeling Surface-Bonded Structures with ABAQUS Cohesive Elements: Beam-Type Solutions

Ted Diehl

DuPont
DuPont Engineering Technology, 101 Beech Street, Wilmington, DE 19880-0840
Ted.Diehl@USA.DuPont.com

Abstract: ABAQUS has implemented a new capability for modeling failure in V6.5 based on a cohesive element formulation. This paper evaluates the modeling of crack initiation and propagation in surface-bonded structures using this new approach. Specifically, the work looks at two generalized test problems: Double Cantilever Beam (DCB) analysis and single-arm peeling of very thin elastic substrates. Comparisons with several analytical and pseudo analytical benchmarks demonstrates how to utilize this new technique as well as the impressive accuracy of the resulting FEA solutions for these highly nonlinear crack propagation and peeling problems.

Keywords: Surface-bonded structures or joints, adhesive joints, cohesive elements, cohesive failure, fracture mechanics, beam theory, double cantilever beam analysis, single arm peel analysis.

1. Introduction

Many modern structures rely on surface-bonding to hold components together. In some cases the bonds are intended to be permanent, but in others they are not. Modern automobiles have a variety of surface-bonded components that a severe crash could fail, jeopardizing structural integrity of the vehicle. If the components are inside the passenger cabin, they could become dangerous projectiles. On a very different scale of complexity are packaging problems such as designing a robust pretzel bag that has sufficient seal-force integrity to survive shipping but will physically open smoothly at a load that can accommodate a broad range of people. Similar challenges are faced when designing a peelable lid on a semi-rigid food container that must survive internal pressure and shipping loads, yet peel open smoothly and cleanly without partially delaminating. These very different classes of products have one thing in common – the need to understand and predict the onset and *propagation* of failure in a bonded joint.

Classical FEA methods for fracture mechanics have been generally unable to analyze such complex problems. In version 6.5 of ABAQUS, a new cohesive element technology has been implemented for both Standard (implicit) and Explicit that enables generalized modeling of crack propagation problems, including the analysis of both crack growth onset and its ongoing propagation through a structure along a defined surface. The scope of this new capability is extremely broad, encompassing many modeling features and options, including the ability to

model both *adhesive* and *cohesive* failures. While the technology is termed "cohesive elements", it can actually be applied to both adhesive and cohesive problems.

Cohesive element technology is fundamentally based on energy principles. The modeling approach relies on a single layer of *cohesive elements* to represent a "bond", adhesive joint or similar construct. The bond can be thick or it can be infinitely thin. To model a bond between two bodies, a one-element-thick layer of cohesive elements are connected, top and bottom, to the adjoining bodies by either sharing common nodes or through a **`*TIE`** constraint. Utilizing the **`*TIE`** approach in conjunction with the *parts and assembly* feature of ABAQUS provides a versatile method to simulating bonding. During the analysis, the cohesive elements carry loads to bond the two parts together until such a point in the solution exists for which conditions mandate the initiation of damage and potentially complete failure within any given cohesive element(s). These criterions are assessed on an element by element basis continually through-out the solution. ABAQUS offers a broad set of cohesive elements features and options to provide the user the ability to specify the criterion for each phase of deformation (elastic, damage initiation, and failure).

2. Generalized Griffith energy criterion

This section provides a brief overview of the generalized Griffith energy criterion used to characterize crack propagation. This will provide a foundation for developing benchmarks and for understanding the underpinnings of the cohesive element approach.

Figure 1a depicts two beams bonded together. The bonding method could have utilized an adhesive such as "glue", ultrasonic welding, conventional welding, thermal bonding via heat sealing, or a number of other technologies. As the tips of the beams are pulled apart, a point in the deformation history arises after which a crack extends through some portion of the bonded area. Performing an energy balance of the system as the crack propagates between states 1 and 2 in Figure 1a requires

$$\Delta U_{\text{ext}} = \Delta U_{\text{int}} + \Delta U_{\text{c}}\,, \tag{1}$$

where ΔU_{ext} represents the energy change from the externally applied load, ΔU_{int} denotes change in stored energy in the two DCB arms, and ΔU_{c} represents the energy released as the crack extends a distance Δa. Normalizing Equation 1 by the beam width b and crack growth Δa, taking the limit as $\Delta a \to 0$, and finally re-arranging yields the classical definitions of the critical fracture energy, G_{c}, of the bond as

$$G_{\text{c}} = \frac{1}{b}\left(\frac{\mathrm{d}U_{\text{ext}}}{\mathrm{d}a} - \frac{\mathrm{d}U_{\text{int}}}{\mathrm{d}a}\right), \tag{2}$$

where it is noted that

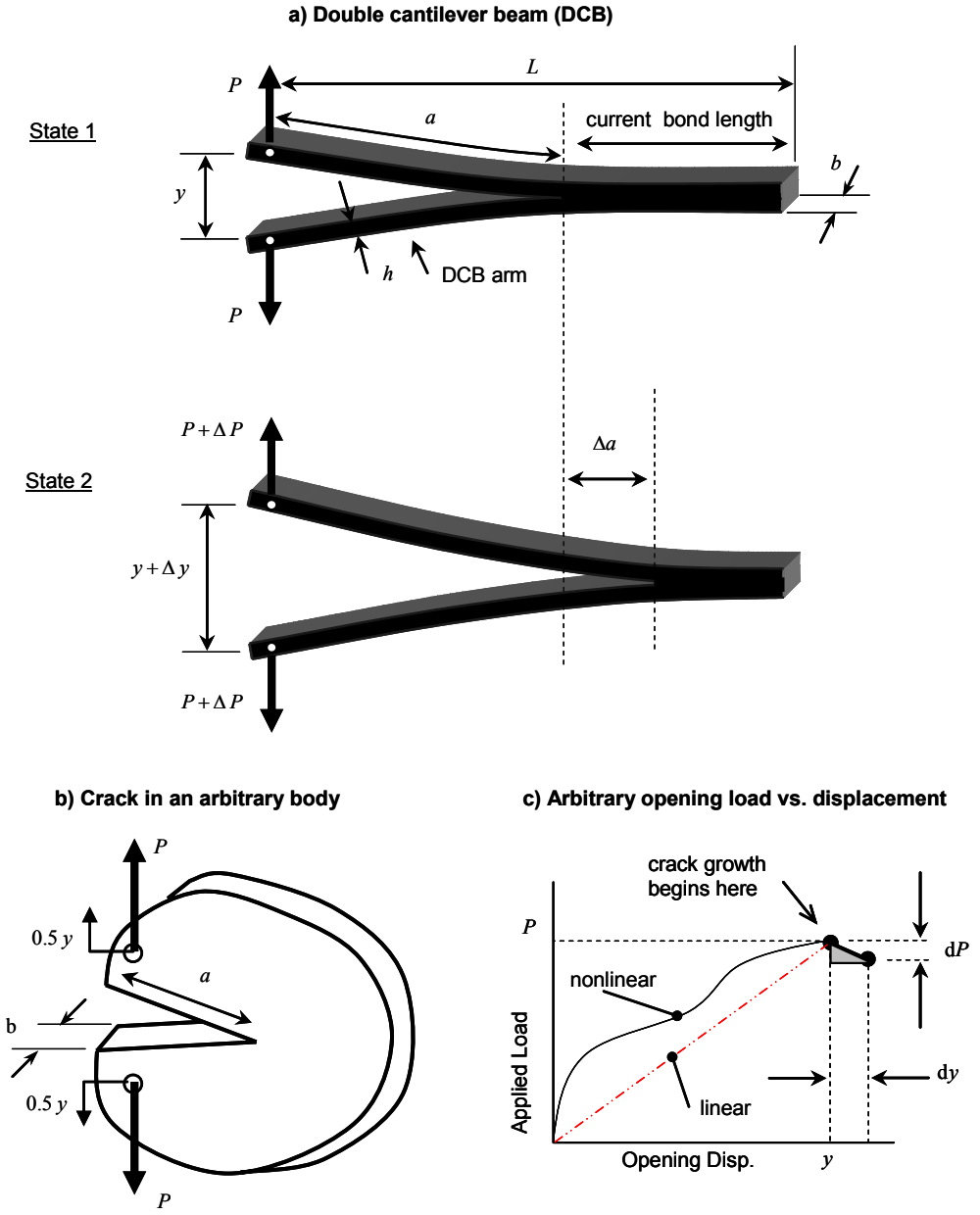

Figure 1. Idealized crack growth in a specimen.

$$G_c = \frac{1}{b}\left(\frac{dU_c}{da}\right). \quad (3)$$

The critical fracture energy, also known as the critical energy release rate, is a material parameter that characterizes the amount of energy a bond or material releases per change of unit crack growth. These equations are equally applicable to general crack growth within a single material (Figure 1b). It is important to note that using this energy-based approach to analyzing the crack, we are implicitly taking a global or smeared approach to the problem, as apposed to a highly local or detailed analysis that is utilized with classical fracture mechanics methods derived around stress intensity factors, singularities, and such.

It is useful to relate the critical fracture energy, G_c, to other quantities such as external loads and displacements of the structure. Figure 1c depicts a generic curve that characterizes the externally applied load, *P,* as a function of opening displacement, *y*. As depicted, the load and displacement increase until such time as the crack begins to grow. Computing the change in external energy due to crack growth from this generic curve, ignoring second order terms, and substituting that result into Equation 2, eventually leads to

$$G_c = \frac{1}{b}\left(P\frac{dy}{da} - \frac{dU_{int}}{da}\right). \quad (4)$$

In general, the internal energy term of Equation 4 can be defined as the sum of elastic and inelastic internal energies. Specific forms relating internal energy to externally applied loads or displacements are problem dependent. Sections 3 and 4 will derive these additional relationships for the two benchmark problems studied.

3. DCB evaluations

3.1 Benchmarks

The DCB benchmarks are derived using the principles of Griffith Energy Criterion and Linear Elastic Fracture Mechanics (LEFM).

3.1.1 LEFM – Linear Elastic Fracture Mechanics

In LEFM analysis, the deformations of the structure (excluding the adhesive or bond) are limited to linear elastic behavior. Furthermore, the bond "material" is assumed to behave with zero ductility until it fails, at which point it releases a finite amount of energy G_c per unit growth of the crack. Under these conditions, we can define the compliance of the structure, *C*, relative to applied load *P* and opening displacement *y* as

$$C = \frac{y}{P}. \quad (5)$$

From Equation 5 the elastic internal energy can be readily computed and after substitution back into Equation 4, we obtain

$$G_{\mathrm{c}} = \left(\frac{P^2}{2b} \right) \frac{\mathrm{d}C}{\mathrm{d}a}, \tag{6}$$

where $\mathrm{d}C / \mathrm{d}a$ represents the change in compliance of the structure as the crack length changes. Equation 6 is valid provided that no inelastic deformation occurs in the structure (excluding the bond material) and that the bond material behaves with zero ductility until it fails, at which point it releases a finite amount of energy G_{c} per unit growth of the crack.

3.1.2 DCB benchmarks based on Timoshenko and Euler beam theories

The compliance of the DCB specimen depicted in Figure 1a can be estimated using classical beam theory. Timoshenko beam theory, which includes the influence of shear flexibility, predicts the DCB compliance as a function of crack length to be

$$C^{\mathrm{Timo}}(a) = 2 \frac{a^3}{3EI} \left(1 + \frac{3 f_s E I}{\mu A a^2} \right), \tag{7}$$

where E and μ are the linear elastic modulus and shear modulus of the DCB arm material, A and I are the cross-sectional area and bending moment of inertia of a single arm in the DCB specimen, f_s is the shear form-factor, and the factor 2 in the beginning of the equation accounts for the fact that we have two identical arms. For beams with rectangular cross-sections and linear elastic materials,

$$f_s = \frac{6}{5}, \quad A = bh, \quad I = \frac{bh^3}{12}, \quad \mu = \frac{E}{2(1+\nu)}. \tag{8}$$

Substituting Equations 7 and 8 into 6 yields

$$G_{\mathrm{c}}^{\mathrm{Timo}} = \frac{12 P^2 a^2}{E b^2 h^3} \left(1 + \frac{(1+\nu)}{5} \left(\frac{h}{a} \right)^2 \right) \tag{9}$$

The derivation shown here is using the same shear flexible beam theory utilized in most ABAQUS beam elements. It is noted that Kinloch and others (Blackman, 2000; BSI, 2001; Kinloch, 1990) have utilized a slightly different version of a shear flexible beam formulation than that shown in Equation 7 and 8. For the cases studied in this paper, the numerical differences between our derivation here and those of Kinloch and others are negligible.

In ABAQUS FEA models, the critical fracture energy G_{c} is an input to the model and P is either a specified boundary condition or a computed result. Solving for P yields

$$P^{\text{Timo}} = \frac{b\,h}{2\,a}\sqrt{\frac{G_c\,E\,h}{3\left(1+\frac{(1+\nu)}{5}\left(\frac{h}{a}\right)^2\right)}} \qquad (10)$$

The opening displacement as a function of crack length is found to be

$$y^{\text{Timo}} = 4\,a^2\sqrt{\frac{G_c}{3\,E\,h^3}}\,\frac{\left(1+\frac{3(1+\nu)}{5}\left(\frac{h}{a}\right)^2\right)}{\sqrt{1+\frac{(1+\nu)}{5}\left(\frac{h}{a}\right)^2}} \qquad (11)$$

Together these two sets of equations predict how the applied load and opening displacement will vary as a function of crack length during crack propagation. In actual physical testing of a DCB specimen, measuring detailed and accurate values of crack growth during a test can be very challenging. It is also quite challenging obtaining crack front propagation data in an automated way from a generic nonlinear FEA model. However, measurement of the applied load vs. opening displacement is readily obtained and generally quite accurate. Unfortunately, manipulating Equations 10 and 11 to arrive at a closed-form analytical representation of P as a function of y is extremely difficult.

Utilizing Euler beam theory, which ignores shear flexibility, results in the following relationship:

$$P^{\text{Euler}} = \frac{b}{\sqrt{y}}\left[\left(\frac{G_c\,h}{3}\right)^3 E\right]^{1/4} \quad \ldots \text{ valid during crack growth} \qquad (12)$$

Equation 12 provides a concise relationship that shows how the different parameters are fundamentally related. It is further noted that prior to crack growth (or after crack growth has been arrested), the load vs. opening displacement relationship is linear (for both theories):

$$P = \frac{y}{C} \quad \ldots \begin{matrix}\text{valid prior to crack growth} \\ \text{or after crack growth arrest}\end{matrix} \qquad (13)$$

Figure 2a shows the Timoshenko-derived prediction of load vs. opening displacement and crack growth vs. opening displacement for a DCB specimen defined by the parameters listed in the figure. The Timoshenko result was computed using Equations 10 and 11 over crack lengths defined from 25.4 mm to 225 mm. A full evaluation of Timoshenko and Euler beam theory demonstrates that for typical DCB specimen geometries there is less than a 5% difference in predicted beam compliance between the two approaches when $a > 5\,h$. For Equations 10 - 12, the response is dependent on the derivative of compliance and therefore is less sensitive, resulting in less than 5% difference when $a > 3\,h$.

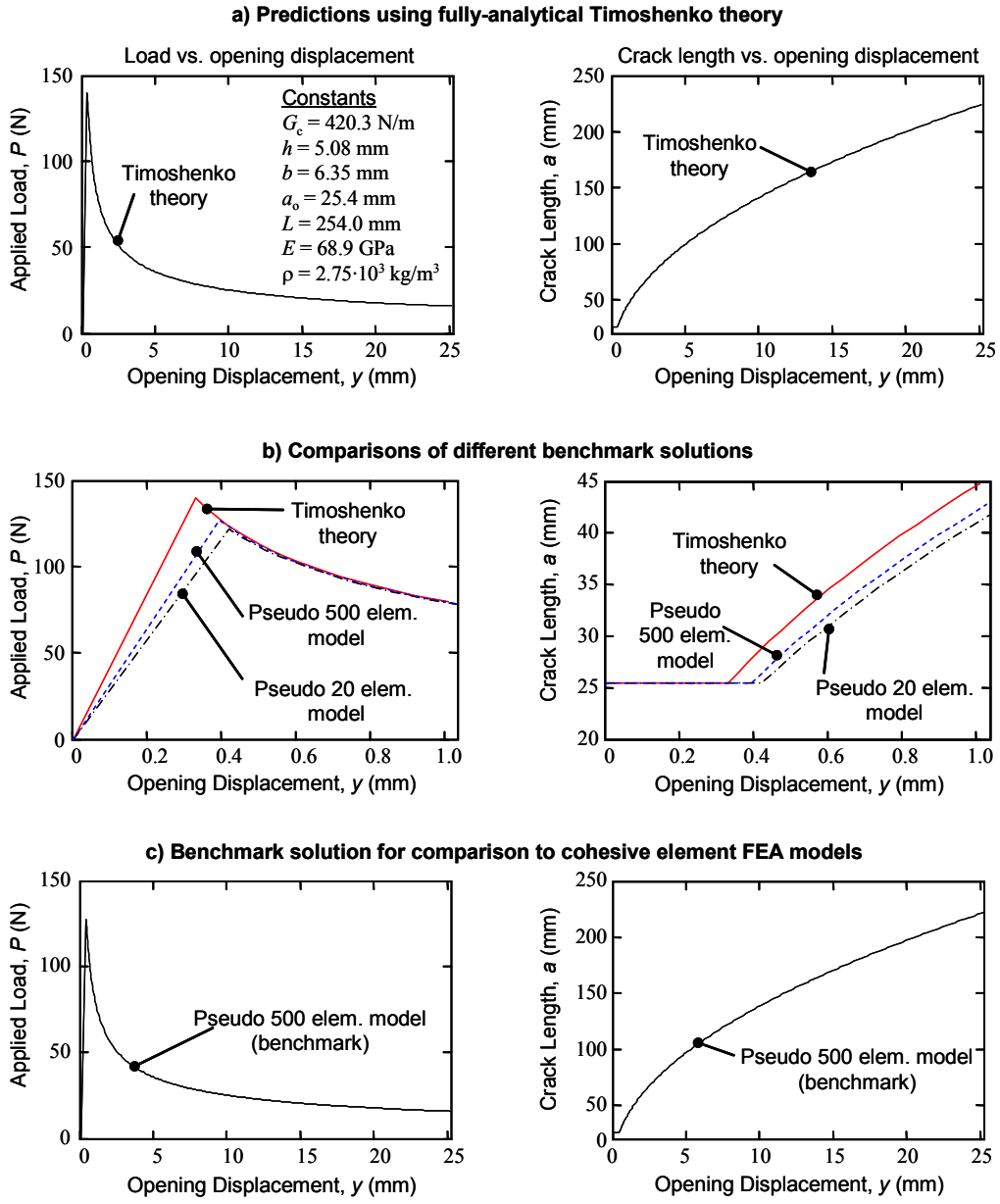

Figure 2. Theoretical benchmarks for DCB analysis.

3.1.3 DCB benchmarks based on pseudo analytical modeling

The theoretical Timoshenko benchmark derived in Section 3.1.2 and plotted in Figure 2a has assumed that the two arms are *ideally* clamped at the root of the crack front in the bond surface. This idealization does not occur in reality because of root rotation caused by local compliance of the surrounding material (Kinloch, 1994). When the DCB is modeled in ABAQUS using cohesive elements to represent the bond, an exact rotation constraint at the root of the crack tip is not imposed either, albeit for a different reason. In ABAQUS, cohesive elements constrain the top and bottom arms together in the bond area by imposing stiffness on displacement degrees of freedom. There is no direct coupling to the rotational degrees of freedom in the beam elements across the bond. Only by successive displacement constraint along the length of the bond area is an effective rotational constraint developed. This behavior is a softer constraint than the idealized constraint imposed in the Timoshenko (or Euler) theory. To address this discrepancy, several linear ABAQUS/Standard models using 2-dimensional, type=B21, beam elements were analyzed to obtain the FEA prediction of beam compliance with displacement-only constraints in the bond area. This data was collected and utilized to numerically derive DCB compliance functions as a function of crack length. Results of these *pseudo* analytical calculations for two different mesh densities are displayed in Figure 2b. Other mesh densities of 50 and 100 elements per arm were evaluated (not shown) and showed that for the DCB dimensions analyzed and successive displacement constraint approach, negligible change in predictions occurred beyond a 500 element (per DCB arm) model. Therefore the *Pseudo 500 elem model* result depicted in Figure 2b and 2c is deemed the *benchmark* to compare the cohesive element solutions against.

It is noted that for the 20 element mesh, imposing rotation constraints at the root tip directly via MPC's produced results identical to the Timoshenko theory. It is also noted that for future studies with continuum element meshes instead of beam element meshes, that this type of pseudo analytical methodology should be employed to derive appropriate benchmarks at that time.

3.2 DCB predictions using cohesive element approach

3.2.1 General modeling approach

Modeling failure, especially surface-bond failure, is a highly nonlinear and complex problem. The nature of the solution is likely to be non-smooth, causing convergence difficulties for Standard and creating noisy solutions with Explicit. ABAQUS/Standard has several numerical stability features to help mitigate some of these problems. Several of the existing ABAQUS-created examples demonstrate this approach.

ABAQUS/Explicit is chosen for the studies here because the explicit dynamics method is considered by the author to be generally more robust for highly non-smooth problems. When analyzing "tricky" or difficult problems, inappropriate selection of model parameters or stabilization penalty values in an implicit method like Standard can result in solutions that fail to converge very early in the solution – providing the analyst with little information to resolve the problem. With Explicit, the analyst can be quite far off in the specification of model and penalty parameters, yet still get a solution. The initial solutions for an ill-defined problem in Explicit may look quite poor, but having any solution at all will give you valuable insight into how to "tune

your way into a viable space" where realistic and accurate solutions are possible. The negative of the Explicit approach is that the analyst must be comfortable with various Digital Signal Processing (DSP) concepts and know how to properly analyze and process very large data sets that are often very noisy.

Our earlier study of arm compliance (Figure 2 and Section 3.1.3) has provided guidance that between 100 and 500 beam elements per arm is a reasonable structural mesh. The elements utilized to bond the two arms together are 2-dimensional, 4 noded, type=COH2D4, cohesive elements. Following traditional FEA techniques, one might initially utilize the same mesh density for the cohesive elements as utilized for the structural beam elements and simply equivalence the regions at their common boundaries. Doing so and then analyzing the progressive failure of the DCB as it peels apart might produce a "zipper effect" in the solution, causing excessively noisy results. In Standard, this might result in severe solution convergence problems. Refining the entire model is one method of reducing the zipper problem, but at the expense of increasing the entire model size and decreasing solution efficiency. A more efficient approach is to employ a concept called *over-meshing*, where by one meshes the cohesive elements with a higher mesh density than the surrounding structural mesh it is adhered to. Implementing this approach requires the use of the **`*TIE`** feature in ABAQUS to connect the mismatched meshes. This approach generally has only a small impact on the *total* size of the model (for a typical real-world model of a bonded structure). For example, if the DCB arms are meshed structurally with 100 beam elements down the length (2.54 mm element length), then a 5x over-meshing would utilize cohesive elements with a length of 0.508 mm (1/5 the beam element length). Studies of cohesive element over-meshing on several classes of problems indicates that 5x is about the right amount in general. Over-meshing at ratios above 5x does not typically improve solution fidelity significantly and only decreases solution efficiency. If the structural mesh is highly refined, then no over-meshing may provide adequate results.

ABAQUS offers a broad set of cohesive elements and features. For modeling surface-bonded structures, the **traction-separation** constitutive response option is recommended. It is intended for cases where the adhesive is very thin, often so thin as to be impractical to accurately define its physical thickness. Bulk material properties of the adhesive are often unknown or not applicable to the analysis. The user even has the option in this approach of modeling an adhesive with zero thickness. The traction-separation constitutive law relates stresses to *separations* in the though-thickness, and transverse shear directions.

Figure 3a shows the general form of the traction-separation material response for cohesive modeling in ABAQUS – a triangle. It is important to note that the law uses the bond separation distance instead of physical strain as the independent axis. It is formulated this way to accommodate the common case of a "zero" thickness bond. The constitutive relationship depicted in Figure 3a is a 1-dimensional relationship. In ABAQUS, the actual behavior is generalized to accommodate 2-d and 3-d analyses (see ABAQUS documentation for additional details). The basic concept in the cohesive element approach is that the cohesive elements carry loads to constrain the two parts together until loads and deformations on the cohesive elements cause damage and failure. When the element has fully failed, it will have accounted for an amount of energy equal to the critical fracture energy defined for the real material. To accommodate this within a finite element framework, the cohesive material must have finite definitions of stress and

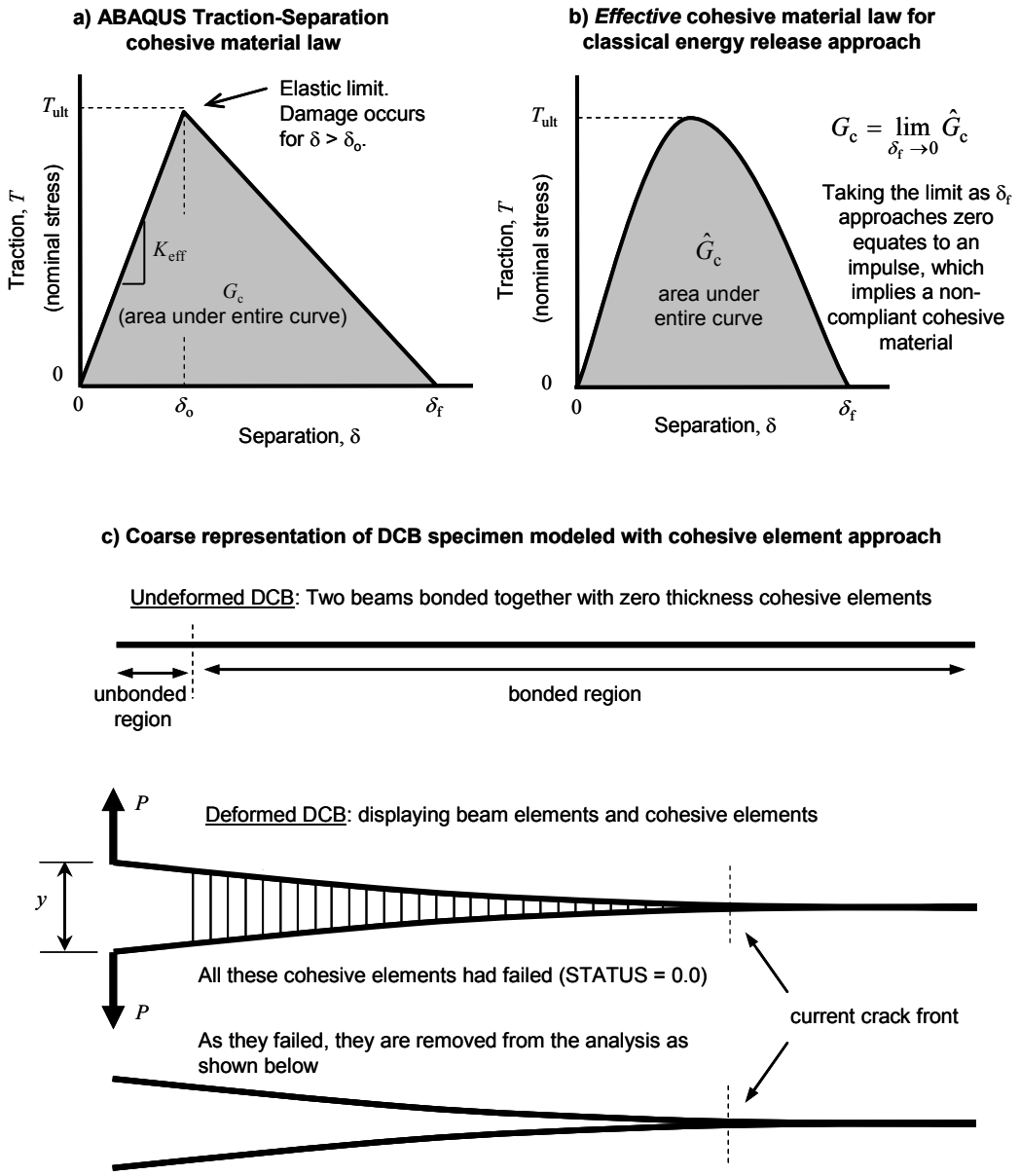

Figure 3. Modeling with cohesive elements.

separation over which the fracture energy can be released. For the triangular law used by ABAQUS, the cohesive element exhibits recoverable linear elastic behavior until the tensile separation has exceeded δ_o, beyond which damage occurs, and ultimately element failure if the separation exceeds the material's failure separation, δ_f. A physical interpretation of this failure separation parameter, δ_f , is that it characterizes the cohesive material's ductility. As such, we will also refer to δ_f as the *cohesive ductility*.

Classical methods of analyzing fracture and peeling assume that the bond or cohesive material is infinitely stiff in its bonding directions until fracture, upon which a finite amount of fracture energy G_c is released. This "rigid" assumption was implicit in the analytical and pseudo analytical benchmarks derived earlier and plotted in Figure 2. Figure 3b, provides an interpretation of this "rigid" assumption within the context of a traction-separation constitutive construct. An impulsive-like behavior is defined as the limit of the cohesive ductility, δ_f, goes to zero (and the ultimate stress goes to infinity), but that the area under the curve remains finite. The cohesive element approach requires the bond to be compliant and have some amount of ductility. There is much debate in the literature about which approach is correct, the cohesive element method or the classical impulsive method. In general, neither is "perfectly correct", as both are engineering representations to complex physical phenomenon. The numerous cohesive element simulations presented in the remainder of this paper will demonstrate that excellent correlation between the two approaches can be achieved.

3.2.2 Setting up the DCB problem in ABAQUS

The DCB problem as defined in Figures 1a and 2 characterizes the bond's behavior with a ***single parameter***, G_c. The simplest surface-bond cohesive model in ABAQUS requires the selection or definition of ***eleven*** ABAQUS input choices. Needless to say, some assumptions must be made! Given no other data, we assume isotropic behavior for the bond. Any repeated inputs shown below imply an isotropic assumption was employed (such as **Gc**, **Gc** below).

The critical fracture energy behavior for the bond is defined via

```
*DAMAGE EVOLUTION, TYPE=ENERGY, MIXED MODE BEHAVIOR=BK, POWER=1.0
Gc, Gc
```

For an isotropic behavior, the BK mixed mode behavior option is the easiest choice to define in terms of input syntax effort. Since we have defined both mode I and mode II critical fracture energies the same (thus isotropic), the value of the related power term (a required input for BK, set to 1.0 here) will have no actual effect on the solution. The resulting cohesive behavior will follow the general triangular behavior depicted in Figure 3a.

The benchmark assumes the bond behaves infinitely rigid until it releases energy upon crack growth, something that we cannot achieve in an exact manner with the cohesive element approach. However, the smaller we set this cohesive ductility number, δ_f, the more the bond will behave like theory, until such time that it causes "numerical" problems. Thus, this term is viewed as a penalty parameter. Utilizing other physical information for the problem, we initially set this failure value, δ_f, to 0.050 times the typical cohesive element mesh dimension of our initial model "D1" (model "D1" parameters are fully described in Section 3.2.3, Figure 4).

The critical fracture energy for the triangular traction-separation law of ABAQUS is related to the material's *effective* ultimate nominal stress T_{ult} and cohesive ductility (failure separation) δ_f via

$$G_c = \frac{T_{ult}\,\delta_f}{2}. \qquad (14)$$

Having defined δ_f, and knowing the value of G_c, we utilize Equation 14 to compute the *effective* ultimate nominal stress T_{ult} of the bond material (another penalty parameter). This data is entered via

```
*DAMAGE INITIATION, CRITERION = MAXS
Tult, Tult, Tult
```

Remember that this is not really the ultimate stress of a bulk version of the bond material. This is simply a penalty parameter. The whole concept of cohesive elements is to avoid trying to resolve the complex, nearly singular stress state that exists at the leading edge of a crack.

Next we must define the initial elastic behavior of the cohesive material. From Figure 3a, the initial material stiffness per unit area (load per unit displacement per unit area), K_{eff}, is simply

$$K_{eff} = \frac{T_{ult}}{\delta_o}. \qquad (15)$$

Defining the *damage initiation ratio* as

$$\delta_{ratio} = \frac{\delta_o}{\delta_f} \qquad (16)$$

provides a simple scalar variable ranging between 0 to 1 (exclusive) for defining when damage initiates. Combining Equations 14 - 16 shows that

$$K_{eff} = \frac{2\,G_c}{\delta_{ratio}\,\delta_f^2}. \qquad (17)$$

The value of the *effective* elastic modulus of the cohesive material E_{eff} is related to K_{eff} via

$$E_{eff} = K_{eff}\,h_{eff}, \qquad (18)$$

where h_{eff} is the initial *effective* thickness of the cohesive element. The user has two options of how this thickness is defined in ABAQUS. One option is to have it defined by the actual geometric thickness defined by the nodal definitions defining the cohesive element (via ***Cohesive Section, Thickness = Geometry**). For many surface bonding applications this approach is highly problematic because the actual physical thickness of the bond (or bond material) is ill-defined or unknown. Another option is to define the geometric thickness (via nodal locations) as zero or any value that is deemed appropriate and then to manually define a constitutive thickness on the ***Cohesive Section** card via the **Thickness = Specified**

option. This later approach is the default method. A useful technique is to specify a *unity* thickness in this case (especially considering the actual thickness is often ill-defined). Doing so means that the effective modulus which is entered on the ***Elastic** card is actually the initial cohesive material stiffness per unit area. It also means that the strains reported in the output database for the cohesive elements are actually the separation values δ.

Noting that the bond in the benchmark is idealized as infinitely thin, we have no physical knowledge of an actual bond thickness. Hence, we define the "nodal" cohesive element thicknesses as zero and utilize a unity value for the user specified thickness h_{eff}.

```
*COHESIVE SECTION, RESPONSE =TRACTION SEPARATION, THICKNESS = SPECIFIED,
ELSET=Glue, Material=bond
1.0,
```

Assuming a damage initiation ratio $\delta_{\text{ratio}} = 0.5$ and utilizing Equations 17 and 18, we can compute the *effective* elastic modulus, E_{eff}, which is then entered via

```
*ELASTIC, TYPE = TRACTION
Eeff, Eeff, Eeff
```

Since we have chosen an Explicit modeling approach, we must supply a material density for the bond. Given the fact that no volumetric density is defined for the bond material in the problem, and the fact that the bond material is assumed to have essentially no thickness, one might reasonably ponder on how to define the bond's mass density! Again, we turn to the penalty concept to arrive at a solution. We simply compute an *effective* density so that the bond material does not, in general, unnecessarily constrain the solution time increment that the problem would otherwise require. The bond's *effective* density, ρ_{eff}, is computed via

$$\rho_{\text{eff}} = E_{\text{eff}} \cdot \left(\frac{\Delta t_{\text{stable}}}{f_{\text{t2D}}\ h_{\text{eff}}} \right)^2 \qquad (19)$$

where the stable time scale factor for 2D cohesive elements is $f_{\text{t2D}} = 0.32213$ (for cohesive elements whose original nodal coordinates relate to zero element thickness) and Δt_{stable} is the initial stable time increment *without* cohesive elements in the model. The value of ρ_{eff} computed in this manner should be checked to make sure that it is not imposing too much mass in the bond area relative to the local mass of the surrounding structural materials. A simple formula to check this is to evaluate the area mass density ratio defined as

$$\rho_{\text{ratio}}^{\text{area}} = \frac{\rho_{\text{eff}}\ h_{\text{eff}}}{\rho_1\ h_1 + \rho_2\ h_2} \qquad (20)$$

where ρ_i and h_i ($i = 1,2$) are the volumetric mass density and local component thickness of the two adjoining structures (DCB arms here). For the cases evaluated by the author so far, Equation 19 has provided satisfactory guidance on setting a penalty value for the bond density, ρ_{eff}.

Lastly, upon complete material failure of a given cohesive element, it is desirable to direct the code to remove the failed element from the solution via

```
*SECTION CONTROLS, NAME=GLUE-CONTROLS, ELEMENT DELETION=YES
```

Allowing failed cohesive elements to remain in the solution frequently created large numerical distortions caused by improper application of bulk viscosity damping on failed elements. This problem has been identified to ABAQUS and should be addressed in a future release. Deleting the elements upon failure caused no ill effects on any of the solutions and avoided this problem.

3.2.3 Numerical results from ABAQUS/Explicit models

Figures 4 - 10 present several different Explicit model results compared to the benchmark defined in Figure 2c. In all cases, the FEA analysis was a pseudo quasi-static analysis computed with Explicit. To simulate a quasi-static problem, the imposed tip opening motions used to drive the models were ramped up and set at a speed to minimize kinetic energy in the model to a sufficiently small value while still yielding acceptable solution efficiency. Most of the models ran between 2 and 20 minutes on a 3.4 GHz Xeon processor running Windows XP.

Most of the figures first display the raw prediction of tip load P vs. tip opening displacement y. To ensure no aliasing has occurred in the collection of this transient data, the solution history output (displacement and reaction load) was recorded at every time increment for each model. Data sets ranged from 20,000 increments to over 300,000 increments. It is noted that ABAQUS now offers a useful antialias decimation filtering option for solution output; enabling significant reduction in the data storage requirements. However, this feature was not utilized here because we desired to see the entire solution first, prior to decimation and low-pass filtering. The other plots commonly displayed in the figures are zoomed views of load vs. displacement around the initial onset of crack propagation (raw and low-pass filtered) and the full view with filtered results. The filtered results utilized a 4 pole, double pass (zero phase) Butterworth IIR filter with end distortion minimization (see Diehl, 2000 for further details on this type of filtering). It is also noted that filtering a result that is intended to have a sharp change will tend to "round-off" the solution a bit. Thus, the filtered results at the transition between the initial linear compliance and the onset of crack growth are lowered slightly by filtering relative to the benchmark. The selection of filter parameters was chosen to minimize this type of distortion while still removing unwanted frequency content from the solution. One could take the more laborious approach of splitting the data at this transition and filtering separately to avoid this small distortion, if desired.

The figures also show predictions of crack growth as a function of opening displacement. This quantity was derived from the field data of each of the models by utilizing a specially designed python script that would search the STATUS variable in all the cohesive elements for each of the 100 output frames utilized for field data. Since the location of the crack front is not expected to have high frequency content, aliasing is not an issue for evaluating the crack growth using only 100 data frames. The script has logic that could identify the crack front based on finding the transition area in the cohesive element mesh where the STATUS changed from 1.0 to 0.0 (0.0 is a fully failed element).

Careful study of the results depicted in Figures 4 - 10 show the following:

1. In general, accurate results are be obtained over a range of meshes and penalty parameters. In several cases, proper use of DSP to remove high frequency solution noise significantly improves results interpretation. See Figure 6 for a strong example of this.

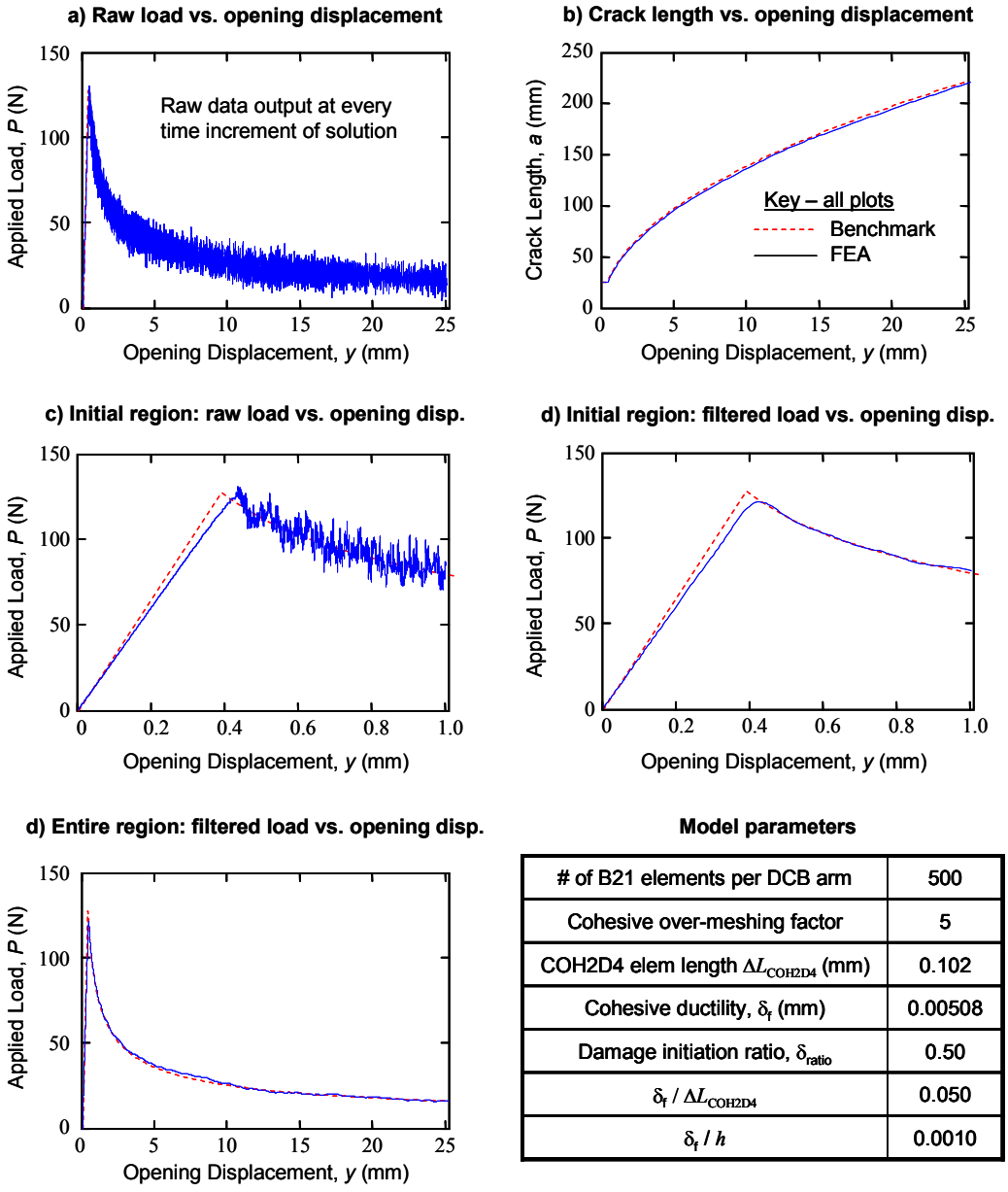

Model parameters

# of B21 elements per DCB arm	500
Cohesive over-meshing factor	5
COH2D4 elem length ΔL_{COH2D4} (mm)	0.102
Cohesive ductility, δ_f (mm)	0.00508
Damage initiation ratio, δ_{ratio}	0.50
$\delta_f / \Delta L_{COH2D4}$	0.050
δ_f / h	0.0010

Figure 4. ABAQUS/Explicit FEA predictions from DCB model "D1". Accurate results obtained with a refined mesh and relatively low cohesive ductility.

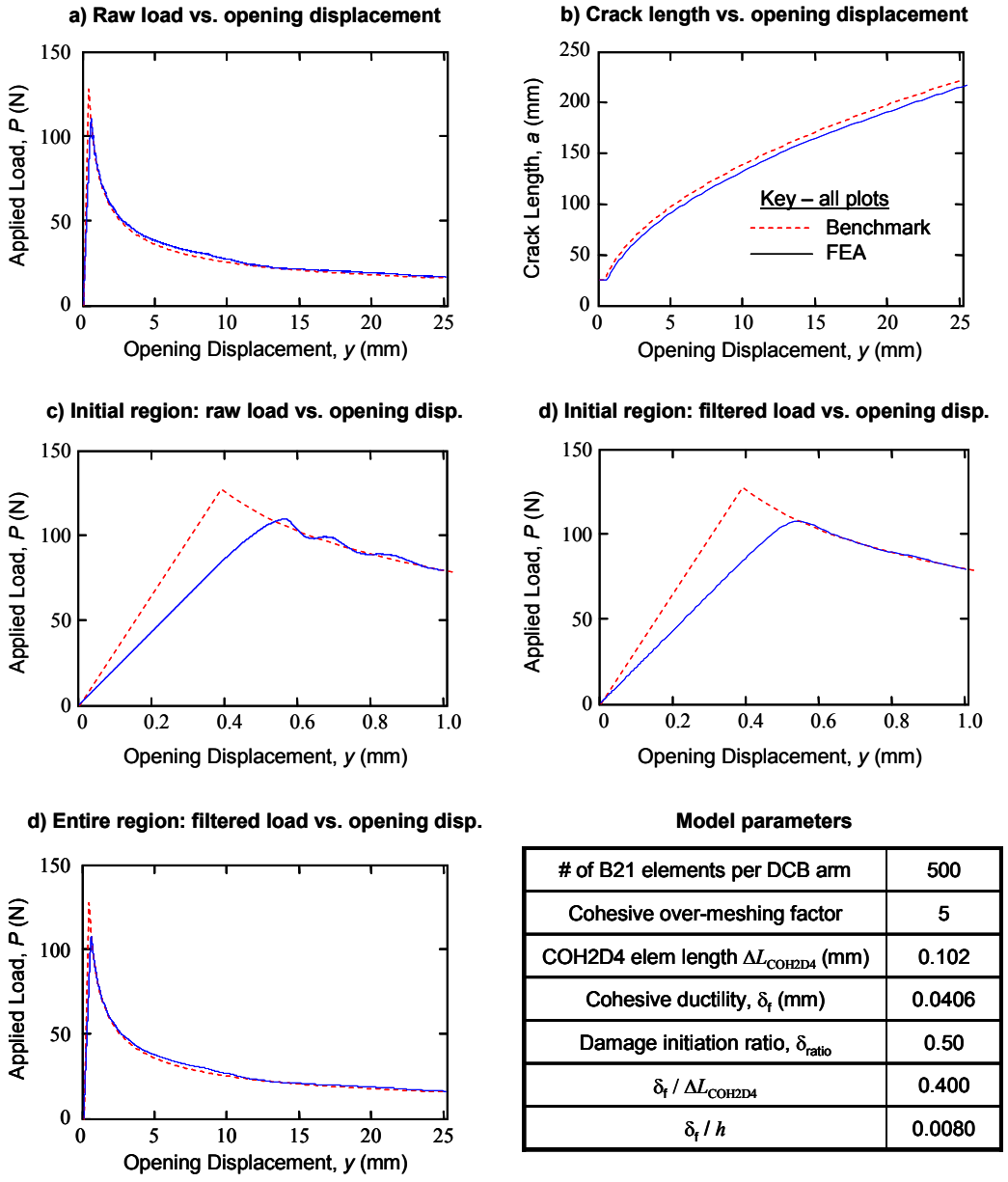

Model parameters

# of B21 elements per DCB arm	500
Cohesive over-meshing factor	5
COH2D4 elem length ΔL_{COH2D4} (mm)	0.102
Cohesive ductility, δ_f (mm)	0.0406
Damage initiation ratio, δ_{ratio}	0.50
$\delta_f / \Delta L_{\text{COH2D4}}$	0.400
δ_f / h	0.0080

Figure 5. ABAQUS/Explicit FEA predictions from DCB model "D2". Demonstrates influence of increasing cohesive ductility (measured absolute and mesh-relative).

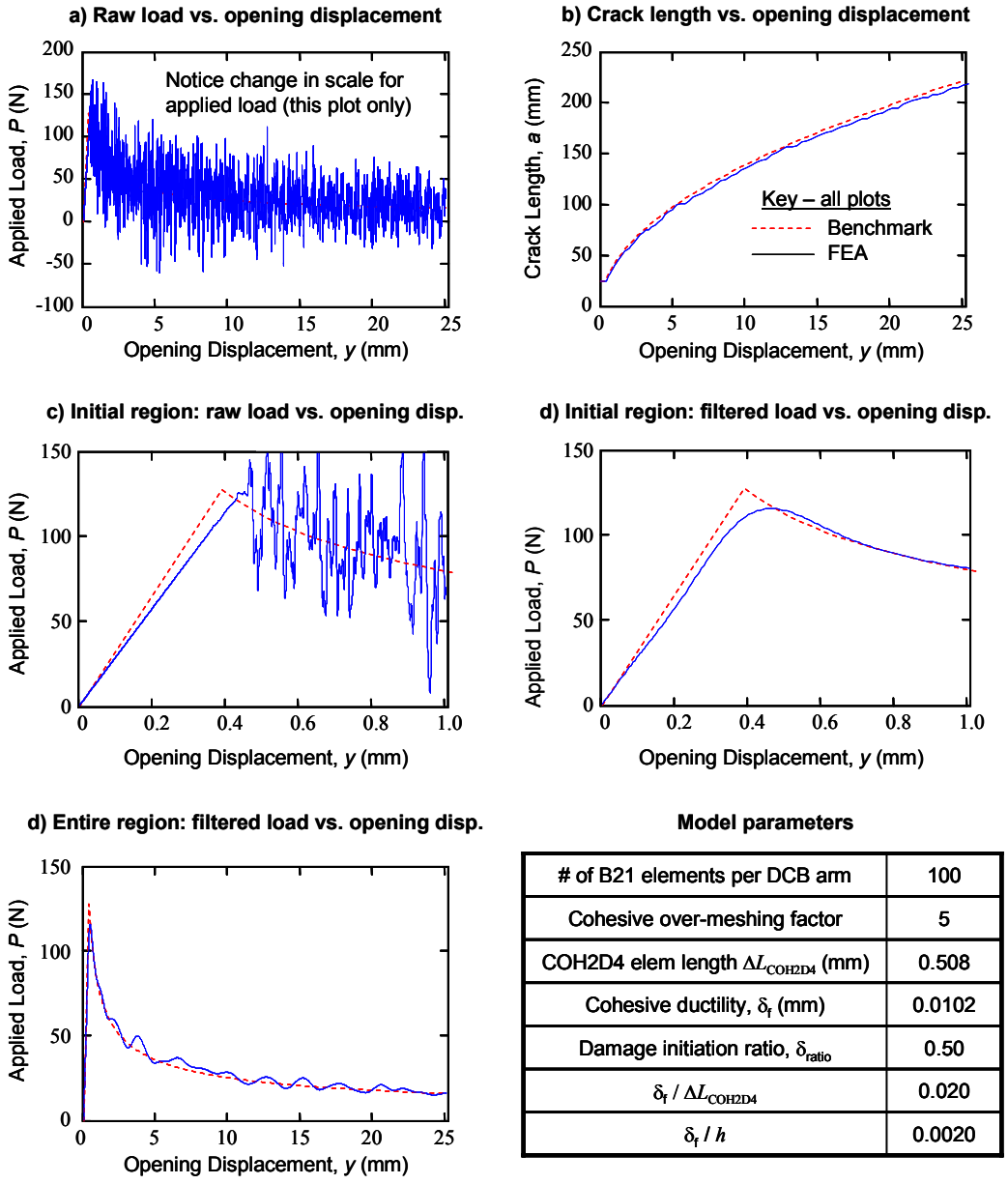

Model parameters

# of B21 elements per DCB arm	100
Cohesive over-meshing factor	5
COH2D4 elem length ΔL_{COH2D4} (mm)	0.508
Cohesive ductility, δ_f (mm)	0.0102
Damage initiation ratio, δ_{ratio}	0.50
$\delta_f / \Delta L_{COH2D4}$	0.020
δ_f / h	0.0020

Figure 6. ABAQUS/Explicit FEA predictions from DCB model "D3". Demonstrates a model near the limit of mesh adequacy relative to the cohesive ductility simulated.

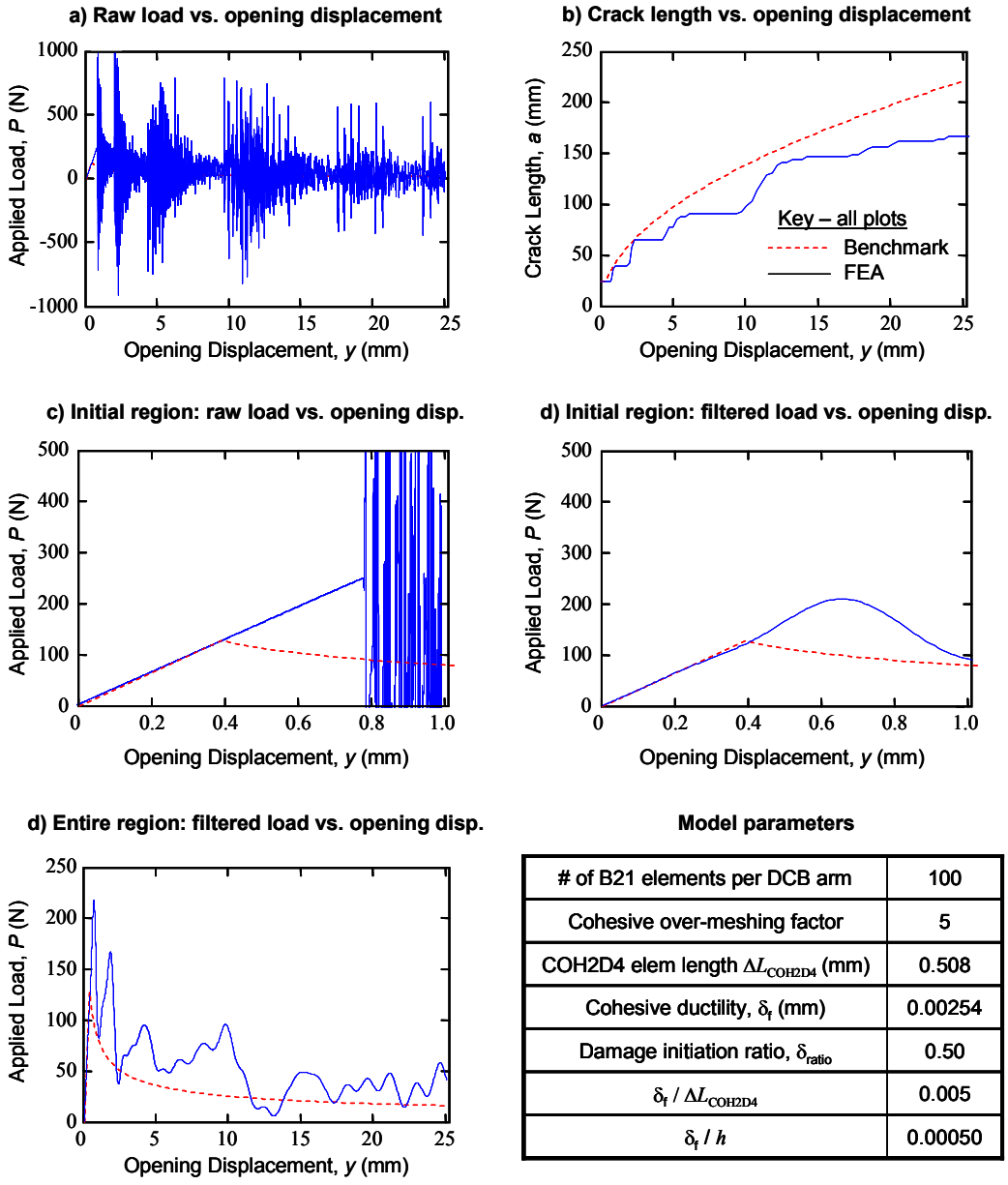

Model parameters

# of B21 elements per DCB arm	100
Cohesive over-meshing factor	5
COH2D4 elem length ΔL_{COH2D4} (mm)	0.508
Cohesive ductility, δ_f (mm)	0.00254
Damage initiation ratio, δ_{ratio}	0.50
$\delta_f / \Delta L_{COH2D4}$	0.005
δ_f / h	0.00050

Figure 7. ABAQUS/Explicit FEA predictions from DCB model "D4". Demonstrates poor results when mesh is too coarse relative to the cohesive ductility simulated.

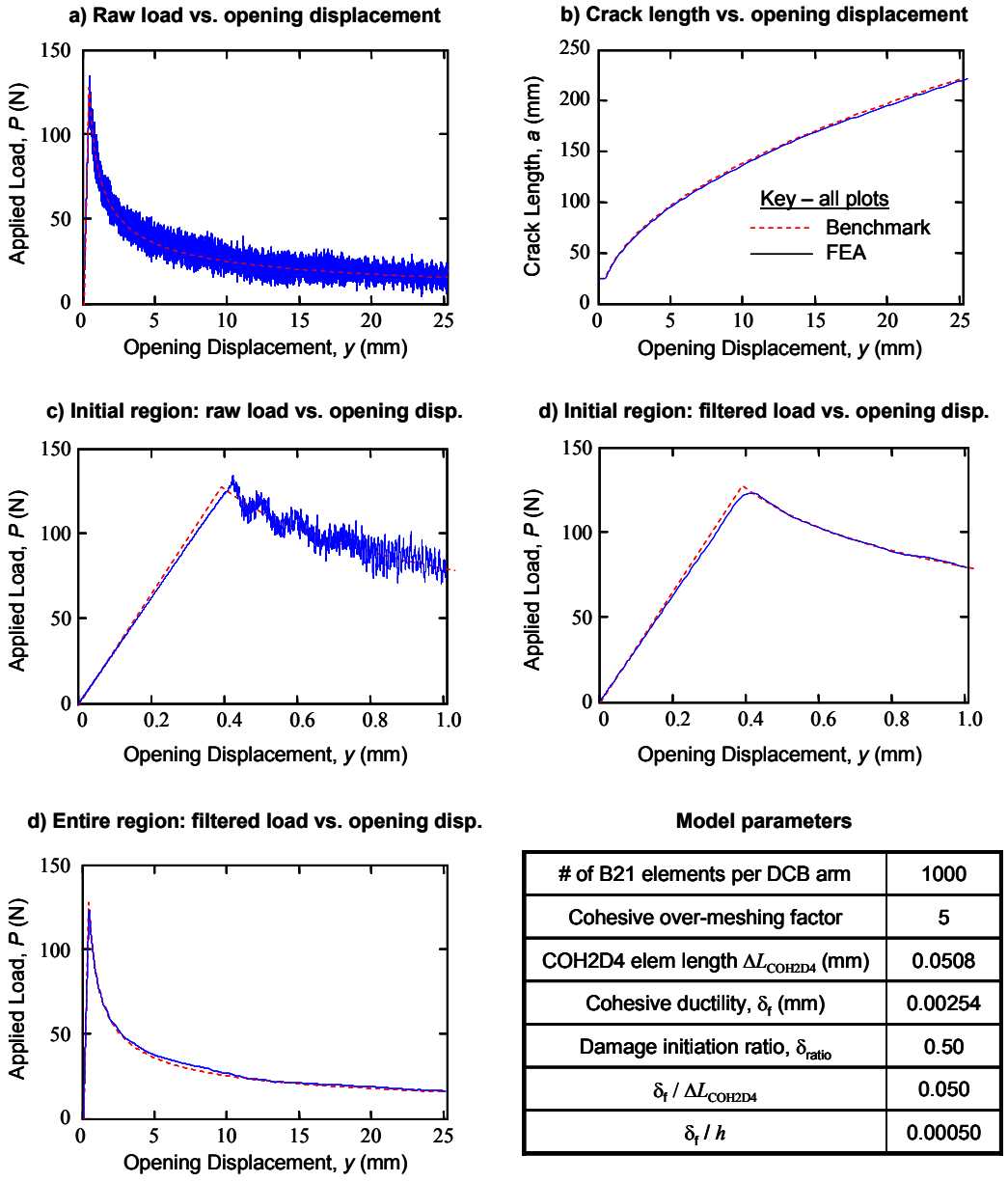

Model parameters

# of B21 elements per DCB arm	1000
Cohesive over-meshing factor	5
COH2D4 elem length ΔL_{COH2D4} (mm)	0.0508
Cohesive ductility, δ_f (mm)	0.00254
Damage initiation ratio, δ_{ratio}	0.50
$\delta_f / \Delta L_{COH2D4}$	0.050
δ_f / h	0.00050

Figure 8. ABAQUS/Explicit FEA predictions from DCB model "D5". Demonstrates an appropriate mesh can achieve accurate results for a very low cohesive ductility.

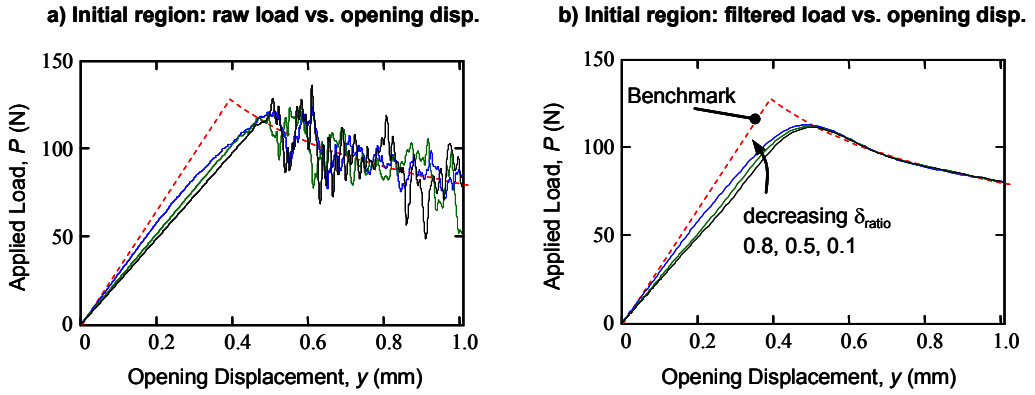

Model parameters

B21 elem's per arm	100		ΔL_{COH2D4} (mm)	0.508	δ_f / ΔL_{COH2D4}	0.040
Over-meshing	5		δ_f (mm)	0.0203	δ_f / h	0.0040

Figure 9. DCB predictions from several Explicit FEA models demonstrating that solutions are insensitive to selection of damage initiation ratio, δ_{ratio}.

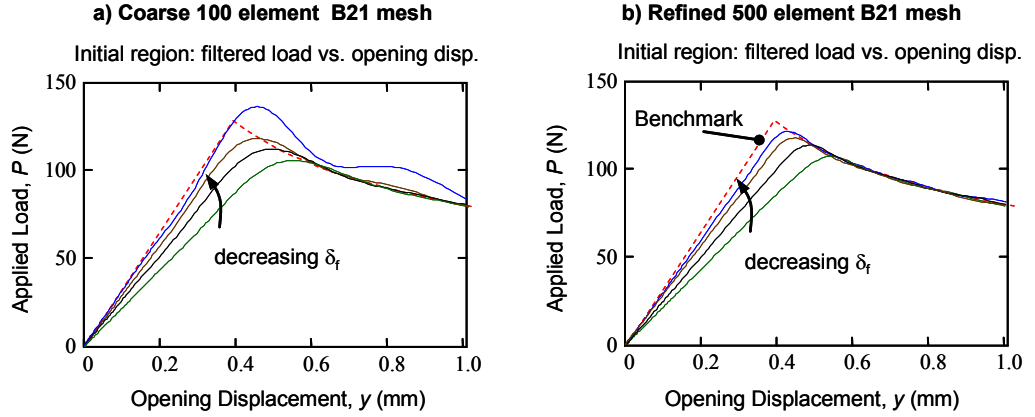

Model parameters

Cohesive over-meshing factor = 5, Damage initiation ratio, δ_{ratio} = 0.5

Decreasing δ_f values shown are 0.0406, 0.0203, 0.0102, 0.00508 (mm)

Figure 10. DCB predictions from Explicit FEA models demonstrating that solutions converge to *ideal,* non-ductile, bond behavior as cohesive ductility is decreased.

2. The mesh-relative cohesive ductility ratio, $\delta_f / \Delta L_{COH2D4}$, is the best measure of assessing the apparent level of the cohesive ductility penalty. When this ratio is set too low, the *relative* ductility of the bond (measured relative to the mesh discretization) becomes too low and the solution quality will degrade significantly because the mesh cannot resolve the compliance gradients sufficiently (Figure 7). Increasing this ratio, either by increasing the mesh density or increasing bond ductility δ_f, improves the solution. There is a reasonable range for which results compare quite well to the ideal benchmark which *assumes* zero bond ductility. Figures 4 - 8 and Figure 10 demonstrate these concepts.

3. A robust indicator of solution fidelity is the smoothness and plausibility of the crack length vs. opening displacement data. If this result was non-smooth, as shown in Figure 7, then no amount of DSP could salvage the solution because the physical behavior of the model was poorly represented. These problems were caused by having insufficient cohesive ductility relative to the mesh discretization supplied in the model. Figure 8 demonstrated that this is easily fixed by increasing the mesh. It could also be addressed by increasing cohesive ductility.

4. Figure 9 demonstrated that the model accuracy was relatively insensitive to the selection of the damage initiation ratio, δ_{ratio}. Close inspection of Figure 9 shows that as δ_{ratio} is decreased (making K_{eff} and E_{eff} stiffer), the model initially behaves stiffer but ultimately curves back , prior to crack growth, to the same result regardless of the value of δ_{ratio}. This nonlinear response prior to crack growth is caused by a blunting effect over a few cohesive elements at the crack front. This also implies that using a pseudo analytical benchmark that attempted to include the initial cohesive stiffness would be inappropriate because of the nonlinear behavior demonstrated in the actual transient solution.

5. Figure 10 demonstrated that the Explicit models were able to converge quite well to the ideal benchmark solution. For models with less cohesive ductility than those shown in Figure 10, such as model "D4" from Figure 7, the initial slope matched the benchmark well, but the fracture onset and propagation would overshoot significantly. Simply reducing the cohesive ductility or increasing the FEA mesh density resolved the problem.

4. Thin strip peeling analysis

4.1 Analytical benchmarks

Figure 11a and 11b depict problem set-up and theoretical solutions to the single-arm peeling of a thin elastic strip that is surface-bonded to a rigid substrate. Unlike the DCB example where the beam arms endure small displacements, the thin elastic arm in a peeling analysis endures very large displacements. However, if the peel arm is thin, the strains can be small enough so that elastic deformation is possible, despite the apparently tight bend that the peel arm makes as it transitions off of the bonded surface. Following an energy-based analysis method, one can derive analytical solutions to the peeling problem depicted in Figure 11. If the peel arm has infinite membrane stiffness and zero bending stiffness, then the steady state peeling load, P_{ideal}, is simply computed as

a) Schematic of peeling problem

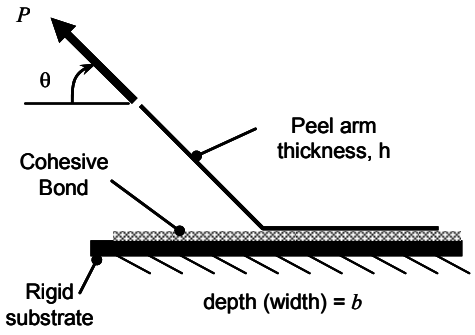

b) Theoretical predictions of steady state peel force

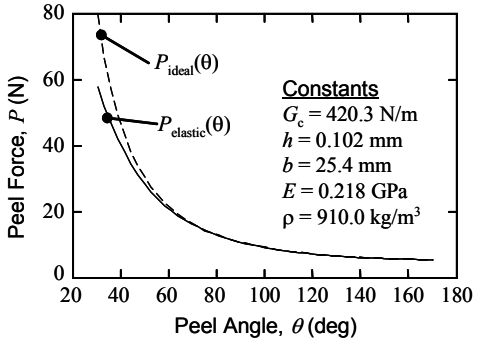

c) Results from three different FEA models

	"S1" - Short Strip, Refined Mesh	"S2" - Short Strip, Coarse Mesh	"S3" - Long Strip, Very Coarse Mesh
Entire strip length (mm)	3.81	3.81	127.0
Total # of beam elements (type= B21)	300	30	300
Cohesive elem over-meshing factor	5	5	5
Cohesive elem length, ΔL_{COH2D4} (mm)	0.00254	0.0254	0.0847
Cohesive ductility, δ_f (mm)	0.0203	0.203	0.676
Cohesive damage initiation ratio, δ_{ratio}	0.50	0.50	0.50
Thickness of peel arm, h (mm)	0.102	0.102	0.102
Mesh-relative ductility, $\delta_f / \Delta L_{COH2D4}$	8.0	8.0	8.0
Cohesive ductility relative to peel arm thickness, δ_f / h	0.2	2.0	6.6
Results Below, Theory = $P_{elastic}(\theta)$			
Peel angle, θ (deg)	**Peel force, theory (N)**	**Peel force accuracy (FEA / theory)**	
30	**57.7**	**0.96**	**0.95**	**0.95**
90	**10.58**	**0.99**	**0.96**	**0.95**
135	**6.23**	**1.03**	**0.97**	**0.97**

Figure 11. Single arm peel analysis – theoretical benchmarks and summary of Explicit FEA predictions using cohesive elements.

$$P_{\text{ideal}} = \frac{G_c\, b}{1-\cos(\theta)} \qquad (21)$$

If the peel arm is assumed to exhibit linear elastic constitutive behavior (both membrane and bending), then the solution of the steady state peeling load, P_{elastic}, becomes

$$P_{\text{elastic}} = b\,h\,E\left[\cos(\theta)-1+\sqrt{(\cos(\theta)-1)^2+\frac{2G_c}{h\,E}}\right] \qquad (22)$$

As demonstrated in Figure 11b, a stretchable peel arm can lower peel forces for shallow peel angles as compared to that predicted from the ideal case (Equation 21).

4.2 Numerical results from ABAQUS/Explicit models

Figure 11c summarizes three ABAQUS/Explicit FEA models of this peeling problem. Each model was run three times to analyze 30º, 90º, and 135º peels. The models are set up similar to the DCB analysis except that only one flexible arm is required. The other side of the cohesive elements is simply constrained from motion to simulate bonding to a rigid substrate. The other significant change relative to the DCB problem is that the thickness of the peel arm is 50x thinner and the modulus is 300x less. The definition of the critical fracture energy is the same, G_c = 420 N/m.

Three different models are presented, two models that are described as short strips (3.81 mm) and one that is a long strip (127.0 mm). Two short strip models are defined, one with a refined mesh and one with a coarse mesh. The results summarized at the bottom of Figure 11c demonstrate that over peel angles ranging from 30º to 135º, ABAQUS/Explicit peel models were able to match the benchmark within 5% or less error in all cases presented.

Figure 12 presents deformed shapes of the thin strip as it is bent up and then peeled at 135º. The peel force vs. time plots of the transient data from the simulation of the short strip, refined mesh is depicted in Figure 12b. Both unfiltered and filtered data is presented. The steady state results tabulated in Figure 11c for the ABAQUS models was obtained by computing the average response of the flat plateau portion of the filtered results. The results in Figure 12c again show how application of appropriate DSP methods can significantly enhance result interpretation.

Figure 13 demonstrates why the long strip "S3" model solution displayed in Figure 12c is so noisy. The mesh is very coarse relative to the tight radius that the thin strip must pass through as it transitions from the flat bonded surface into the peel arm.

Looking at the model inputs summarized in Figure 11c, we see that for all three models the mesh-relative ductility of the bond, $\delta_f / \Delta L_{\text{COH2D4}}$, was kept constant. This allowed us to obtain similar peeling performance for all three models in general. The significant noise shown for the very coarse, long strip model "S3" in Figure 12c is not caused by zippering of the cohesive elements, but rather by the "chain-link unraveling-like" behavior caused from a coarse structural mesh that cannot properly simulate the very tight bend radius that a 135º peel requires. When this model was run at 30º, its solution was nearly as noise-free as the "S1" result for the same angle.

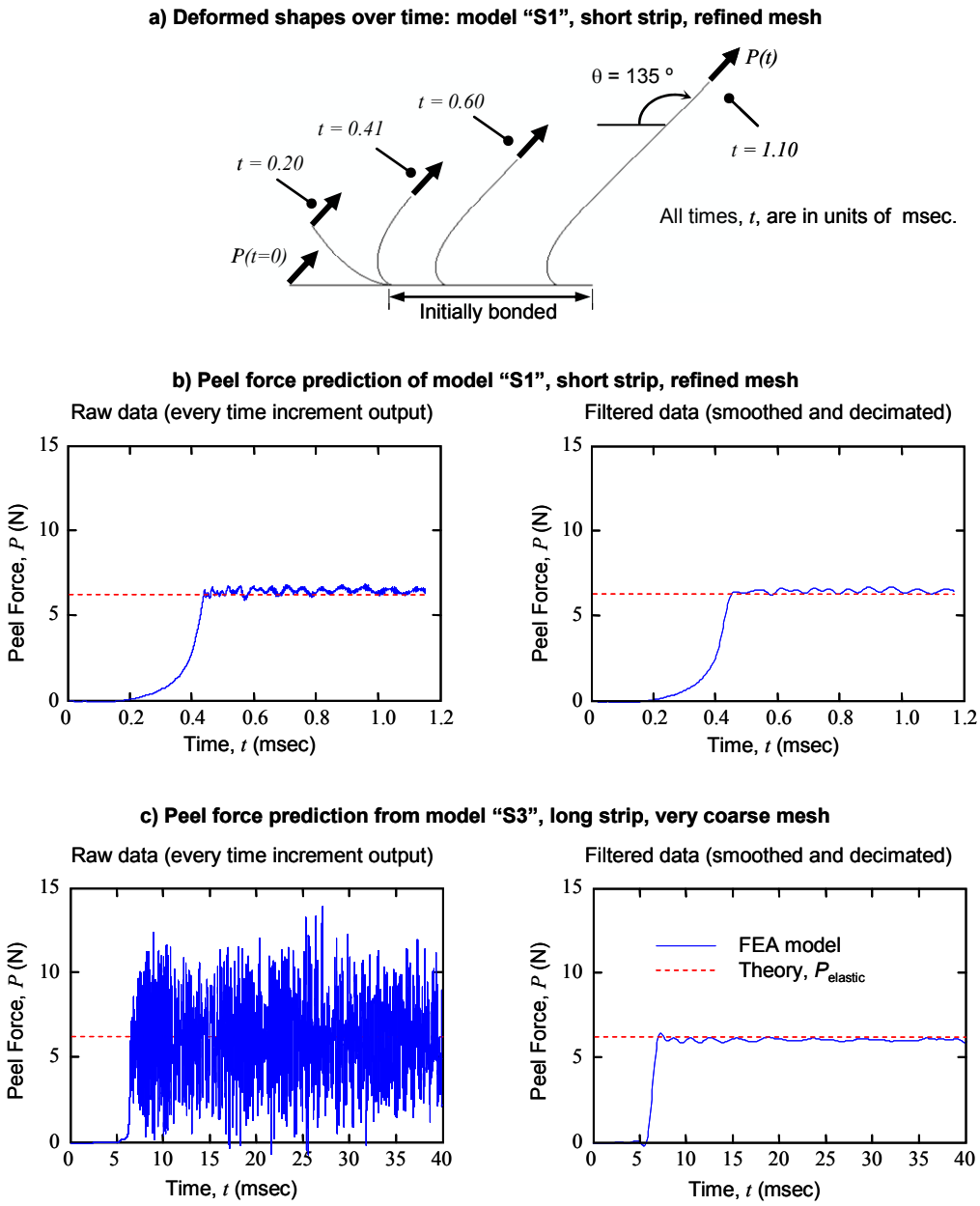

Figure 12. Explicit FEA predictions of 135º peeling of a thin elastic film. Results shown for two very different modeling scales: a short strip modeled with a refined mesh and a long strip modeled with a very coarse mesh.

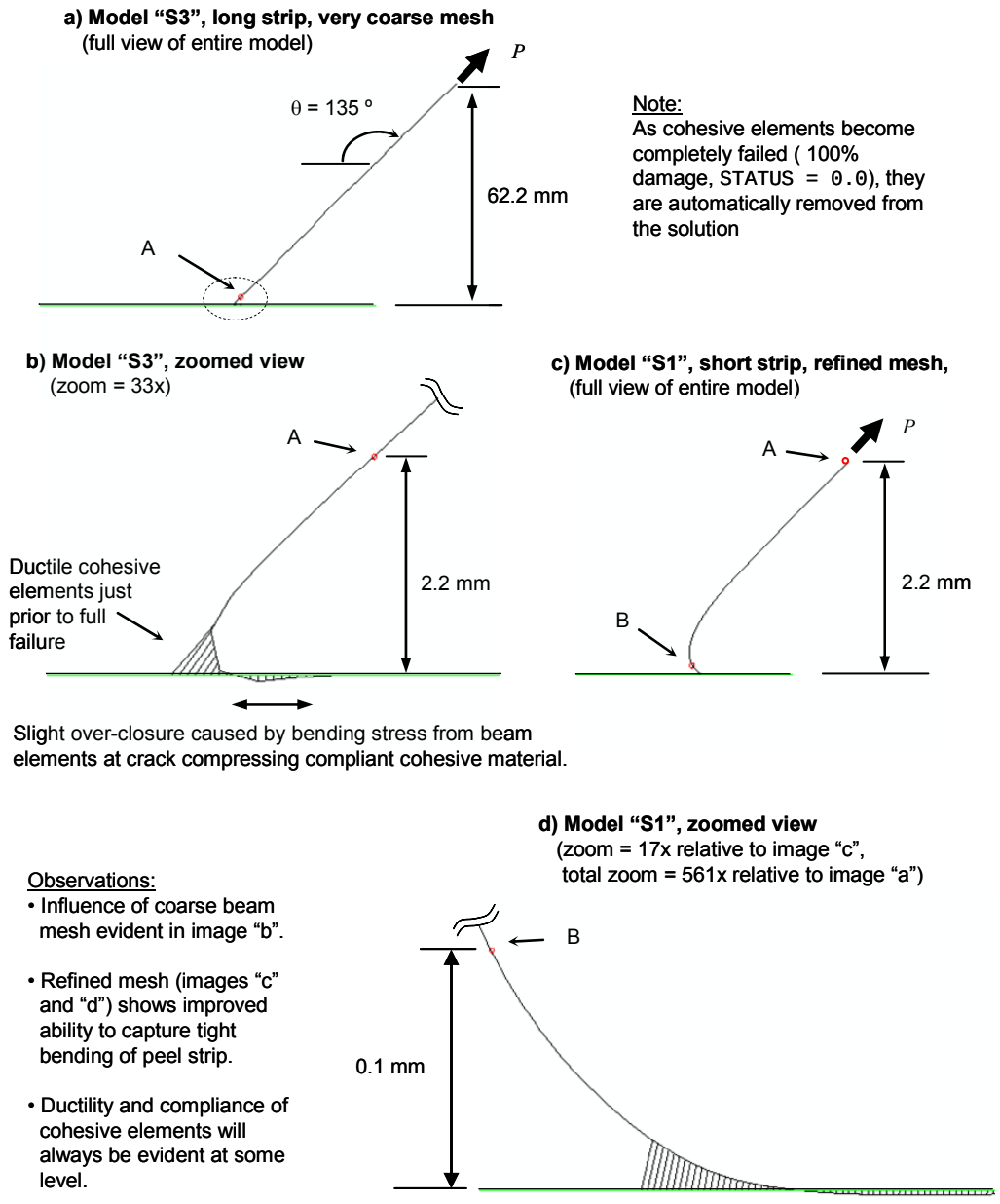

Figure 13. Demonstrating how mesh size relative to physical problem dimensions influences the behavior around the crack front in a thin film peeling analysis.

It is noted that the absolute value of the mesh-relative cohesive ductility ratio, $\delta_f / \Delta L_{COH2D4}$, for the peel models required a value of around 8.0, where as the DCB analysis utilized a value around 0.05. This large difference is due to the very different nature of the two classes of problems. The easiest way to arrive at the appropriate value for this penalty is to test models with a range of values. For particular problems, certain physical characteristics can provide guidance into defining initial starting points for the values.

A last point to make about the peel models presented in this section. If peel arm plasticity is included, then the very coarse long strip model "S3" would produce very poor results because such a coarse model would not properly account for the bending plasticity that the peel arm would need to endure as it made the tight radius. It is expected that the refined, short strip model "S1" would provide much more reasonable results for plastic peel arm behavior.

5. Other comments and observations

This section provides a few other brief comments and observations that have been made during this work. For half symmetric models, the bond or adhesive will only release *half* of the energy since only half of the physical bond is being modeled. To simulate this, you will need to make the following modifications to your cohesive material model inputs:

$$G_c^{sym} = \frac{G_c}{2}, \quad h_{eff}^{sym} = \frac{h_{eff}}{2}, \quad \delta_f^{sym} = \frac{\delta_f}{2}, \quad \rho_{eff}^{sym} = \frac{\rho_{eff}}{2}. \tag{23}$$

All the other quantities such as T_{ult} are computed as defined previously with the appropriate substitution of the four symmetric versions of the quantities defined by Equation 23.

In the problems demonstrated in this work, the value of G_c was given. A reasonable question to ask is "how does one get the value of G_c, especially when it often is not published or otherwise known?" Some adhesives are very complex, exhibit rate effects, mode dependency, etc. For these complex materials, the numerous isotropic and quasi-static assumptions employed here may not be applicable. However, for many surface-bonded applications they are sufficient. In those cases, one can utilize the closed-form equations presented as starting points to estimate the value of G_c for a given material if it is tested using either a DBC protocol or a peel test protocol. Then by using more detailed FEA models using cohesive elements, you can improve your estimate of the critical fracture energy via iterative FEA studies. Using this approach, one can also incorporate additional real-world aspects of the problems such as plasticity of peel arms in thin peel analysis, something that few closed-form methods are able to accommodate in general. It is noted that Kinloch (1994) has some analyses programs that can do this type of analysis under certain circumstances.

Lastly, a significant advantage of using the DSP technology with Explicit is that it allows the user to utilize relatively coarse, fast computing models. For comparisons, many of the coarser models ran 20+ times faster than the more detailed models. On real-world problems that might run for 1 – 5 hours of computation time, a 20x difference is significant!

6. Conclusions

This study has presented impressively accurate simulations of failure in surface-bonded structures using the new cohesive element technology in ABAQUS. A rationale has been shown for how to relate classical energy release methods which assume zero cohesive compliance to the compliance-based method implemented in ABAQUS. A practical approach has been derived and demonstrated to address the problematic issue of determining numerous cohesive element properties when only a single input is known, the critical fracture energy G_c. It was shown that for isotropic cohesive behavior, the cohesive element properties can be resolved down to two primary variables: the critical fracture energy G_c and a penalty parameter defining the cohesive ductility. It was further shown that sizing the cohesive ductility penalty must be done relative to the level of detail desired in the model (mesh density). Additionally, it was demonstrated that employing DSP technology significantly enhanced the interpretation of originally noisy simulation results.

7. References

1. BSI, "Determination of Mode I Adhesive Fracture Energy, G_{IC}, of Structural Adhesives using the Double Cantilever Beam (DCB) and Tapered Double Cantilever Beam (TDCB) Specimens", British Standard BS 7991:2001, October 23, 2001.

2. Blackman, B. R. K., Kinloch, A. J., *Protocol for the Determination of Mode I Adhesive Fracture Energy, G_{IC}, of Structural Adhesives using the Double Cantilever Beam (DCB) and Tapered Double Cantilever Beam (TDCB) Specimens*, Version 00-08, European Structural Integrity Society, June 22, 2000.

3. Broek, D. *Elementary Engineering Fracture Mechanics,* Martinus Nijhoff, 1986.

4. Diehl, T., Carroll, D., Nagaraj, B., "Applications of DSP to Explicit Dynamic FEA Simulations of Elastically-Dominated Impact Problems," Shock and Vibration, Vol 7, pp. 167-177, 2000.

5. Kinloch, A. J., *Adhesion and Adhesives*, Chapman and Hall, 1990.

6. Kinloch, A. J., Hadavinia, H., et. al., "The Peel Behavior of Adhesive Joints," *Proc. of the Annual Meeting of the Adhesive Society*, 2000, 23rd edition.

7. Kinloch, A. J., Lau, C. C., and Williams, J. G., "The Peeling of Flexible Laminates," *International Journal of Fracture,* 66, pp 45-70, 1994.

8. Acknowledgment

The author is very grateful to ABAQUS developers Kingshuk Bose, David Fox, and Harry Harkness for their technical interactions throughout this project. The initial discussions with Tony Kinloch from the Imperial College, London provided a sound start to this project. The support and interactions of DuPont colleagues Mark A. Lamontia, Clifford Deakyne, Delisia Dickerson, Leo Carbajal, Jay Sloan, David Roberts and James Addison is also recognized. The author greatly appreciates the specialized Python script written by James Henderson, DuPont.